Nanoscale

Accepted Manuscript

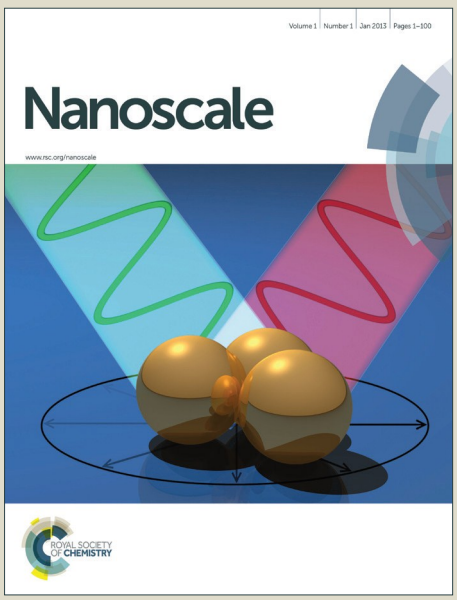

ROYAL SOCIETY OF CHEMISTRY

www.rsc.org/nanoscale

Journal Name

ARTICLE

Experimental and theoretical investigation of a mesoporous K_xWO_3 material having superior mechanical strength†

Received 00th January 20xx,
Accepted 00th January 20xx

DOI: 10.1039/x0xx00000x

www.rsc.org/nanoscale

Sonal Dey,*[‡a] Sean T. Anderson,[a] Robert A. Mayanovic,[a] Ridwan Sakidja,[a] Kai Landskron,[b] Berenika Kokoszka,[b] Manik Mandal,[b] and Zhongwu Wang[c]

Mesoporous materials with tailored properties hold great promise for energy harvesting and industrial applications. We have synthesized a novel tungsten bronze mesoporous material (K_xWO_3; x ~0.07) having FDU-12 type pore symmetry and a crystalline framework. *In situ* small angle x-ray scattering (SAXS) measurements of the mesoporous $K_{0.07}WO_3$ show persistence of a highly ordered meso-scale pore structure to high pressure conditions (~18.5 GPa) and a material with remarkable mechanical strength despite having ~35% porosity. Pressure dependent *in situ* SAXS measurements reveal a bulk modulus κ = 44 ± 4 GPa for the mesoporous K_xWO_3 which is comparable to the corresponding value for the bulk monoclinic WO_3 (γ-WO_3). Evidence from middle angle (MAXS) and wide angle x-ray scattering (WAXS), high-resolution transmission electron microscopy (HR-TEM) and Raman spectroscopy shows that the presence of potassium leads to the formation of a K-bearing orthorhombic tungsten bronze (OTB) phase within a monoclinic WO_3 host structure. Our *ab initio* molecular dynamics calculations show that the formation of the OTB phase provides superior strength to the mesoporous $K_{0.07}WO_3$.

Introduction

With an annual consumption of ~1.8 billion metric tons, synthetic zeolite nanoporous (pore size < 2 nm) materials have a strong impact in the global industry.[1] Consequently, mesoporous (pore size of 2 – 50 nm) materials also have the potential to play a significant role in applications that are critical to the future of our society, such as in heterogeneous catalysis, ion-exchange, gas sensing, and energy harnessing.[2–6] In addition, specially designed mesoporous materials have potential for applications requiring multi-functionality, such as having light weight and high mechanical and thermal stability (e.g., space delivery vehicles). The nano-scale porous structure affords high surface area to volume ratio that generally enhances catalytic, adsorptive, and other physicochemical properties of mesoporous materials. The key requirements of porous materials in extreme-environment applications are substantial thermal, hydrothermal and mechanical stability. Initial studies of these materials suggest that the mechanical stability of silica-based mesoporous materials is directly impacted by the mesoporosity.[5,7,8] However, a full understanding of how the chemical composition, topology and symmetry of the host structure and the mesoporosity govern the stability and mechanical properties of mesoporous materials has yet to emerge. Realizing the full potential of advanced energy systems, whether in high-temperature solid oxide fuel cells, supercritical water biomass gasification, or steam cracking of petrochemicals, requires a materials-by-design approach.

Highly ordered mesoporous WO_3 is a promising material for extreme-environment (e.g., energy harvesting) applications. WO_3 is an indirect band gap semiconductor having visible light response and highly suitable electrode potential characteristics (e.g., for water oxidation).[9] The incorporation of alkali atoms within WO_3 produces non-stoichiometric compounds, namely, alkali tungsten bronzes (M_xWO_3; M = K, Na, Li etc.), having remarkable physical properties depending upon the type of alkali and concentration x.[10–12] Each alkali atom donates an electron to the 5d levels of the conduction band of M_xWO_3 resulting in metallic-like and often superconducting properties.[13–16] The crystalline structure of M_xWO_3 has long intercalation channels that promote efficient transport of alkali ions under the influence of an applied electric field.[17] Of particular interest is a resistivity anomaly that depends upon composition and which functions much like a charge density wave.[13] Whereas periodic mesoporous WO_3 has successfully been synthesized in the past,[9,18–20] tailoring these materials for applications has not been widely addressed. This is especially critical where the

[a] Department of Physics, Astronomy & Materials Science, Missouri State University, Springfield, MO 65897, USA.
[b] Department of Chemistry, Lehigh University, Bethlehem, PA 18015, USA.
[c] Cornell High Energy Synchrotron Source, Wilson Laboratory, Cornell University, Ithaca, NY 14853, USA.
† Electronic Supplementary Information (ESI) available: experimental details of SEM and TEM measurements, SAXS data analysis, procedure for Rietveld refinement, peak fitting for Raman results, the modelling approach, UV-Vis and N2 sorption measurements. See DOI: 10.1039/x0xx00000x
* sdey@sunypoly.edu
‡ Current address: Colleges of Nanoscale Science and Engineering, State University of New York Polytechnic Institute, Albany, NY 12203, USA

porosity compromises the mechanical stability of mesoporous WO_3.

Here we report the first detailed experimental and *ab initio* modeling investigation of the structural and mechanical properties of a novel crystalline FDU-12 type mesoporous K_xWO_3 material consisting of highly ordered pore structure (~ 9 nm dia.). From *in situ* small angle x-ray scattering measurements made on our specimens, we show that periodic FDU-12 type mesoporous K_xWO_3 (x ~ 0.07) has exceptionally high stability under high pressures. By using a combination of *ab initio* molecular dynamics, molecular dynamics simulations and our experimental results, we show that the mechanical stability of mesoporous $K_{0.07}WO_3$ is significantly enhanced by the incorporation of K and the resultant formation of hexagonal rings of WO_6 octahedra surrounding the alkali within an orthorhombic tungsten bronze (OTB) phase that helps to stabilize and strengthen the framework of the material.

Experimental section

Synthesis of Mesoporous $K_{0.07}WO_3$

The synthesis of periodic mesoporous $K_{0.07}WO_3$ was made using a nanocasting method. The novel $K_{0.07}WO_3$ was synthesized according to procedures based on preparation of mesoporous WO_3 from another silica material, KIT-6, described in the literature.[21] In the first step, cubic large-pore periodic mesoporous silica LP-FDU-12 (19 nm pore size) was prepared using a soft template, and in the second step, this material was used as a hard template in nanocasting of tungsten oxide. The preparation of LP-FDU-12 involves use of KCl, which is the source of K in the final mesoporous tungsten oxide product. For the synthesis, 0.5 g of FDU-12 was placed into a two-necked flask and the flask was evacuated for 2 hours. Then, a solution of 0.8 g of phosphotungstic acid hydrate ($H_3PW_{12}O_{40}$) in 14 g of ethanol was added and the mixture was stirred in vacuum for 48 h (during this process, phosphotungstic acid infiltrates into the FDU-12 pores). After stirring, the prepared mixture was put into a petri dish and kept in an oven at 40 °C for a day to evaporate ethanol. Next, a temperature treatment of the prepared white powder at 500 °C for 5 hours led to the formation of a K-bearing WO_3/FDU-12 composite. Removal of the FDU-12 template was done by stirring the powder with 5% HF solution for 6 hours, followed by a centrifugation and washing of the powder with distilled water and drying for overnight in a vacuum oven.

In situ x-ray scattering experiments

The *in situ* small angle and wide angle x-ray scattering experiments were made at the B1/B2 beamline of the Cornell High Energy Synchrotron Source (CHESS) at pressures up to 18.5 GPa using a diamond anvil cell (DAC). A Re gasket with a hole of diameter 250 µm and thickness of 125 µm was placed between the culet faces of two diamond anvils and filled with the K_xWO_3 mesoporous material. The pressure measurements were made at room temperature using Ar gas as the pressure medium. A small ruby crystal was placed inside the DAC along with the sample and the shifts in the characteristic fluorescence lines of ruby were used to calculate the pressure. A monochromatic radiation of energy 25.51 keV (λ = 0.48608 Å) was incident on the sample in the DAC along the compression axis. The incident beam was collimated to a circular spot of ~100 μm in diameter at the location of the sample. The scattered x-ray photons were collected using a MAR345 detector, with 100 μm^2 pixel area and a total pixel count of 3450 × 3450. The detector was placed at a distance of 1134.562 mm from the sample allowing collection of data to ~3.25 $Å^{-1}$ in the Q-space ($Q=4\pi\sin\theta/\lambda$; θ is the scattering angle). The x-ray spectrometer was calibrated using a CeO_2 standard (NIST SRM 674b). The two dimensional image data were analyzed using the Fit2D software.[22]

Procedures for the analyses of the x-ray scattering data, Rietveld refinement, scanning (SEM) and transmission electron microscopy (TEM) characterization, SEM energy dispersive x-ray spectroscopy (SEM-EDX), Raman spectroscopy, and *ab-initio* (AIMD) and classical molecular dynamics (MD) simulations are discussed in detail in the ESI.

Results and discussion

The TEM and SEM images (Fig. 1a and inset of Fig. 1b) show the spherical pore morphology associated with FDU-12 type mesoporous materials[23] indicating a highly periodic meso-scale order and uniform pore size distribution of the specimen. The SEM-EDX spectrum in Fig. 1b shows presence of K, W and O in the material. The estimated atomic percentages (K ~1.7%, W ~24.4% and O ~73.9%, yielding a formula of $K_{0.07}WO_3$) indicates low overall occupancy of the intercalation sites in mesoporous $K_{0.07}WO_3$.[24,25] High-resolution TEM (HR-TEM) images in Fig. 1c show that the crystallinity of the framework persists after the sample has been under pressure to

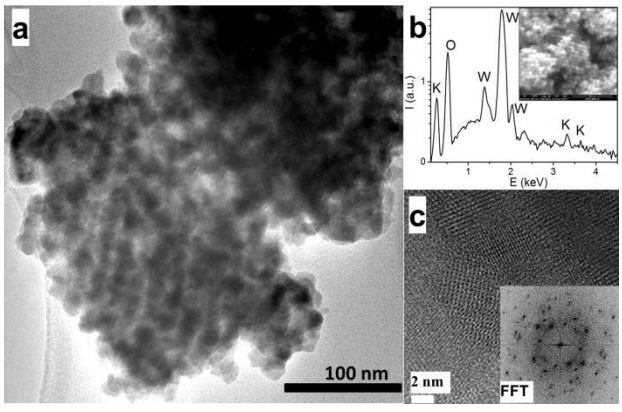

Fig. 1 (a) TEM image of the as-prepared mesoporous $K_{0.07}WO_3$ showing spherical pore morphology; (b) SEM image (inset) and SEM-EDX spectrum showing presence of the K, W and O; (c) A HR-TEM image and its fast Fourier transform (FFT) (inset) showing crystallinity in the sample after applying pressure ~18.5 GPa.

~18.5 GPa. The pore size for this mesoporous material is ~9.4 nm (from TEM) with an average pore wall thickness of ~3 nm. This is in general agreement, when taking into account the presence of both micro- and meso-pores in the material, with analysis of N_2 adsorption/desorption isotherms measured from mesoporous K_xWO_3 using density functional theory (DFT), which yields a narrow pore-size distribution with a pore size of ~12.5 nm (see ESI).

The mesoporous K_xWO_3 was confirmed to be an FDU-12 type material from our SAXS data (inset of Fig. 2a), having a face-centered cubic pore structure (*Fm-3m* symmetry) with a unit cell parameter of 17.0 ± 0.4 nm at ambient conditions. Thus, ~35% of the volume of mesoporous $K_{0.07}WO_3$ consists of pore (i.e., free) space. Fig. 2a shows the fractional change in the volume of the pore-structure unit cell (V_P/V_0) as a function of pressure. The pressure-dependent SAXS data measured from the sample are shown in the inset of Fig. 2a. The pressure ranges are divided into HP-A, HP-B and HP-C regions, as shown in the Fig. 2a, in similar fashion as reported previously.[26] The same pressure ranges are also indicated in Fig. 2b, which shows the x-ray scattering data beyond the SAXS measured as a function of pressure from the sample. Three SAXS peaks are observed which progressively diminish with pressure. Although substantially diminished in intensity, the second reflection peak is observed even at the highest pressure (~18.5 GPa) of measurement. The persistence of (diminished) higher order reflections is indicative of a quasi-long range order of the pores.[27] As shown in Fig. 2a, the mechanical response of periodic mesoporous $K_{0.07}WO_3$ is elastic to ~4 GPa and inelastic at higher pressure values. The linear fit made to the elastic region of the V_P/V_0 data yields a remarkably large value for the bulk modulus $\kappa = 44 \pm 4$ GPa, which is comparable to the measured value of bulk monoclinic WO_3 ($\kappa = 44.5 \pm 0.9$ GPa).[28] Additional *in situ* SAXS measurements have revealed that our mesoporous $K_{0.07}WO_3$ also exhibits excellent stability under extreme hydrothermal conditions (to 400 °C and 0.2 GPa); the results from this study are in preparation and will be published elsewhere.[29]

Fig. 2b shows the x-ray scattering intensity originating from the crystalline framework of mesoporous $K_{0.07}WO_3$. The region between $Q = 1.2$ Å^{-1} to 1.6 Å^{-1} is the middle angle x-ray scattering (MAXS) regime and the region above 1.6 Å^{-1} is the wide angle x-ray scattering (WAXS) regime. The variations in the WAXS across HP-A–HP-B–HP-C regions indicate subtle changes in the symmetry of the host structure with pressure. This reorganization of the atomic-scale structure is directly correlated with the quasi long-range order variations in the meso-scale structure evidenced in the SAXS vs. pressure plot (Fig. 2a). Upon increasing the pressure from 0.9 to 1.8 GPa (HP-A to HP-B), a subtle transition is manifested in the WAXS by the vanishing of some peaks and emergence of new peaks and by a disappearance of the third peak and a marked diminution of the second peak in the SAXS. Thus, the HP-A to HP-B transition is manifested by a marked reduction in quasi long-range pore-structure order of mesoporous $K_{0.07}WO_3$ associated with pore shrinkage with increasing pressure. A similar subtle high-pressure transition is perceived from the

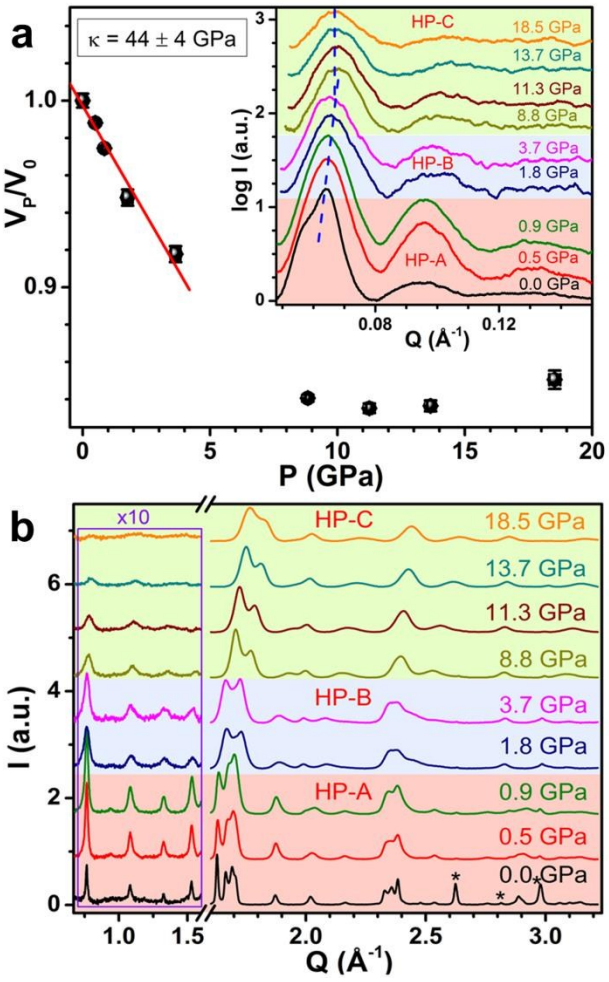

Fig. 2 (a) Fractional change in the pore-structure unit cell volume (V_P/V_0) vs. pressure as calculated from SAXS; the inset shows the background-subtracted SAXS measured from the sample to 18.5 GPa; (b) Background subtracted MAXS (x10) and WAXS data vs. pressure.

WAXS upon increasing pressure from 3.7 to 8.8 GPa (HP-B to HP-C). However, in this case a clear HP-B to HP-C transition is not manifested in the SAXS. In general, the structural order of the material associated with the MAXS is consistent but diminishes with increasing pressure. Similar evolution of pressure-dependent Raman data has been reported in micro- and nano-crystalline WO_3, whose origin is yet to be determined.[26,30,31] One marked difference is the HP-A to HP-B transition discovered for the mesoporous $K_{0.07}WO_3$: This has not been reported from the Raman results for micro- or nano-crystalline WO_3.[26,30,31] The HP-B to HP-C transition is consistent with the HP-1 to HP-2 transition reported from pressure-dependent Raman measurements of WO_3 nanowires.[31]

The contribution from the surface energy of nanomaterials in influencing phase transitions at high pressures (i.e., promotion to higher transition values) has been noted previously.[30,31] It is possible that the meso-scale composition of the host structure (consisting of fused nano-sized crystalline

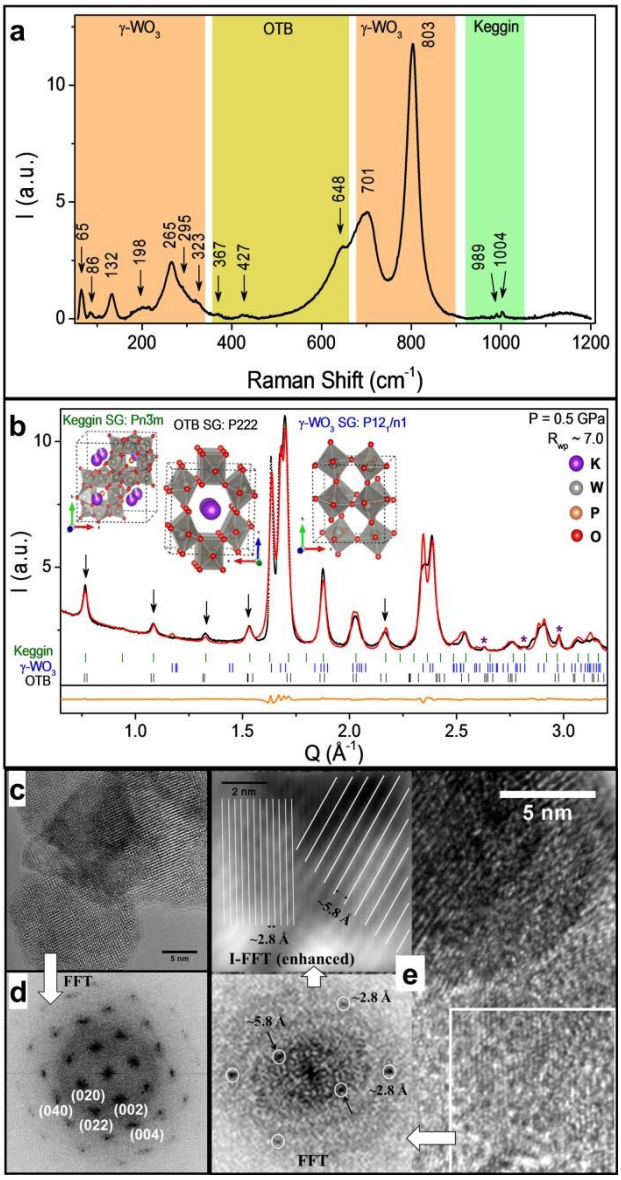

Fig. 3 (a) A Raman spectrum of mesoporous $K_{0.07}WO_3$; (b) Rietveld refinement of the XRD data collected from mesoporous $K_{0.07}WO_3$ at 0.5 GPa. The peaks marked with arrows are due to the K-bearing phases and the '*' to the Re gasket; (c) A HR-TEM image; (d) it's FFT (indexed to $P12_1/n1$ structure) of the γ-WO_3 phase. The zone axis is along [100]; (e) HR-TEM image of the OTB phase (in white square) and the FFT (left) and the enhanced inverse FFT (I-FFT); both are consistent with the OTB structure (*P*222). The I-FFT clearly shows the orthorhombic (010) planes with d ~5.8 Å.

grains) and/or the presence of K in the WO_3-based matrix of the material provides for the origin of the new HP-A to HP-B transition in mesoporous $K_{0.07}WO_3$. Analysis of UV-Vis absorption spectra measured from mesoporous $K_{0.07}WO_3$ reveals an optical band gap of 2.7(1) eV for the material (see ESI). This value is in general agreement with slight energy band gap widening due to quantum-size effects of WO_3 nanoparticles embedded in the pores of mesoporous silica,[32] which is consistent (in addition to HR-TEM data) with a nano-scale morphology of the framework of mesoporous $K_{0.07}WO_3$. Given that this is the first atomic- to meso-scale study of the mechanical and structural properties, further experiments are required to fully understand the origin and nature of the subtle high-pressure phase transitions evidenced in mesoporous WO_3-based materials.

The MAXS (Fig. 2b) is indicative of a superstructure in mesoporous $K_{0.07}WO_3$. Such superstructures have been observed in bulk tungsten bronzes (TB).[24,25,33,34] The presence of a TB phase in mesoporous $K_{0.07}WO_3$ is also supported by Raman measurements shown in Fig. 3a. The Raman bands occurring in the ~100 – 350 cm^{-1} and ~700 – 800 cm^{-1} regions are attributed to the monoclinic γ-WO_3 phase.[35,36] Our results in the ~350–680 cm^{-1} range are in excellent agreement with the lattice dynamics calculations and experimental measurements of Raman bands made from a bulk $Cs_4W_{11}O_{35}$ hexagonal tungsten bronze.[36] Thus, the Raman bands occurring in the ~350–680 cm^{-1} range are attributed to vibrations within the hexagonal rings of WO_6 octahedra of a TB phase. The weak bands in the 950 – 1050 cm^{-1} region are attributed to a Keggin-like $K_3PW_{12}O_{40}$ phase.[37] Symmetry mode Rietveld refinement[38–40] (Fig. 3b) of the MAXS and WAXS measured from mesoporous $K_{0.07}WO_3$ at 0.5 GPa were made using Topas.[41] The 0.5 GPa XRD data was chosen for structure refinement in order to avoid the complication of potentially coexistent monoclinic and triclinic phases in the sample, as was shown for bulk WO_3 wherein a triclinic component transforms to monoclinic at ~0.3 GPa.[30] Rietveld structural refinement is consistent with the Raman data and indicates a mixture of an orthorhombic TB (OTB) (*P*222), a monoclinic γ-WO_3 ($P12_1/n1$) and a $K_3PW_{12}O_{40}$ (*Pn-3m*) phase present in mesoporous $K_{0.07}WO_3$ (see ESI). The OTB phase results from the incorporation of K^+ ions into vacant intercalation sites surrounded by hexagonal rings of WO_6 octahedra. Our HR-TEM images (Fig. 3c-e) also reveal the presence of the OTB phase in mesoporous $K_{0.07}WO_3$. As shown in Fig. 3c and 3d, the majority of the regions found in TEM images are of monoclinic WO_3. However, there are isolated regions that exhibit structure and fast Fourier transform (FFT) patterns consistent with the OTB phase (Fig. 3e). The small atomic percentage (~1.7%) is consistent with fractionation of K^+ ions in isolated regions giving rise to an OTB phase.

We have carried out AIMD calculations and MD simulations in order to provide better insight into the mechanical properties of mesoporous $K_{0.07}WO_3$. Fig. 4a shows our AIMD results for V_P/V_0 vs. pressure in the elastic region for monoclinic (γ-WO_3), hexagonal WO_3, orthorhombic WO_3, and hexagonal $K_{0.33}WO_3$ in comparison to the same quantity determined experimentally from mesoporous $K_{0.07}WO_3$. Our calculations indicate that the bulk modulus κ of γ-WO_3 (κ is given by the inverse of the slope of the linear fitted line) is comparable to that of mesoporous $K_{0.07}WO_3$. However, both of these κ values are substantially smaller than those of hexagonal WO_3, orthorhombic WO_3, and hexagonal $K_{0.33}WO_3$ (see ESI for table of κ values). Our MD simulations shown in Fig. 5a reveal that the bulk modulus has an exponential

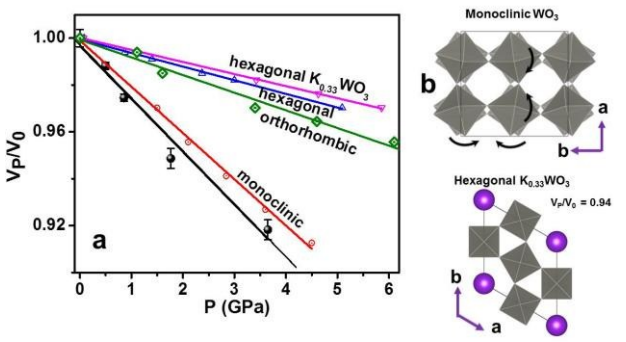

Fig. 4 (a) AIMD calculated V_P/V_0 values for indicated structures compared to data (black) measured from mesoporous $K_{0.07}WO_3$ vs. Pressure; (b) Calculated structural projections showing uniform compression of the hexagonal $K_{0.33}WO_3$ and torsional buckling of the WO_6 octahedra within γ-WO_3 unit cells under pressure.

dependence on the degree of porosity in a manner consistent with the behavior of non-periodic and randomly porous materials.[42] Based on our calculations, mesoporous γ-WO_3 having ~35% porosity (without the OTB phase) is expected to exhibit a greater than 75% reduction in the bulk modulus compared to that of bulk material (i.e., κ is expected to be < ~11 GPa).[28]

Our first principles calculations provide insight into the mechanisms of elastic deformation under hydrostatic pressure for different structural phases and help to understand why mesoporous $K_{0.07}WO_3$ possesses such high mechanical stability under high pressures. The primary difference in the atomic-level structural response is in the torsional buckling of the WO_6 octahedra in γ-WO_3 that is absent in the other phases (see Fig. 4b). Whereas the calculated structural projections show a uniform compression of the hexagonal $K_{0.33}WO_3$ (as well as orthorhombic and hexagonal WO_3) unit cell under pressure, the WO_6 octahedra within the monoclinic WO_3 unit cell rotate in one orientation in one plane (when looking down the *c* axis) and in the opposite direction in the plane immediately underneath the first one (Fig. 4b). The incorporation of the K^+ ions leads to the formation of an OTB superstructure phase and hexagonal rings of WO_6 octahedra surrounding the K^+ ions in mesoporous $K_{0.07}WO_3$, thereby helping to increase mechanical stability against hydrostatic compression in the material. Additional AIMD calculations of the minor $K_3PW_{12}O_{40}$ phase show that this material has a much lower bulk modulus (37.5 GPa) than the orthorhombic or tungsten bronze phase and is therefore not expected to help lower the compressibility of the material (see ESI). Thus, the combination of AIMD calculations and MD simulations show that despite having ~35% porosity, the K-bearing OTB phase has a direct bearing in increasing the mechanical stability of the mesoporous $K_{0.07}WO_3$. This is supported by the evidence in the MAXS signal, showing a much weaker shift in Q than the WAXS signal, with increasing pressure (Fig. 2a (inset) and Fig. 2b).

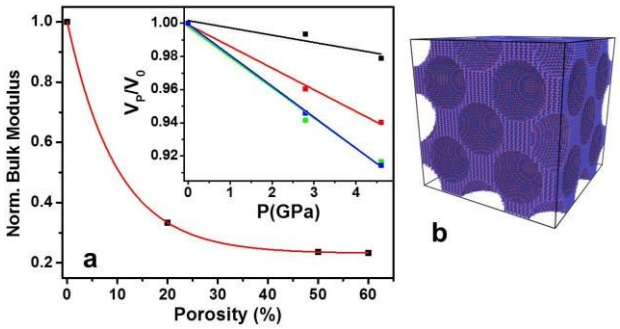

Fig. 5 (a) MD simulation results for the normalized (to bulk value) bulk modulus vs. %-porosity of mesoporous WO_3; (b) an MD simulation box of mesoporous WO_3 with 60% porosity.

We conjecture that the nano-scale composition of the host structure may also contribute to the enhancement of the mechanical stability of mesoporous $K_{0.07}WO_3$. The periodic arrangement of fused nano-sized crystalline grains constituting the framework may provide for additional strengthening of the material. The nano-scale grain boundaries may inhibit plastic deformation by limiting the generation and movement of dislocations in mesoporous $K_{0.07}WO_3$.[43] It should not be difficult to incorporate a greater percentage of alkalis into a WO_3-based framework thus producing hexagonal tungsten bronze and other mesoporous M_xWO_3 materials. Based on our AIMD calculations, we predict that a mesoporous hexagonal TB $K_{0.33}WO_3$ will make for a highly incompressible yet lightweight material, *i.e.*, it will possess a bulk modulus several times greater than mesoporous $K_{0.07}WO_3$ of similar porosity and pore symmetry. In addition, mesoporous hexagonal TB K_xWO_3 should be highly electrically conducting, light weight and highly stable making it ideally suited for fuel cell, battery and other energy harvesting applications.

Conclusions

Our *in situ* SAXS results indicate that a novel periodic FDU-12 type mesoporous $K_{0.07}WO_3$ has remarkably robust mechanical stability under high pressures. Despite having ~35% porosity, the bulk modulus of mesoporous $K_{0.07}WO_3$ is 44 ± 4 GPa, which is very similar to the value reported for bulk monoclinic WO_3 (κ = 44.5 ± 0.9 GPa).[28] Analysis of the MAXS and WAXS data, along with HR-TEM and Raman evidence, shows that the incorporation of intercalated K^+ ions results in the formation of an orthorhombic tungsten bronze (OTB) phase and hexagonal rings of WO_6 octahedra in the host structure. Our first principles modeling shows that the presence of the OTB phase directly impacts the atomic-scale deformation in mesoporous $K_{0.07}WO_3$, resulting in a porous material having high mechanical stability under high pressure conditions. The modification of the host structure of periodic mesoporous WO_3 through incorporation of alkalis has potential for the development of advanced materials-by-design that possess multi-functionality.

Acknowledgements

S.D., S.T.A., R.A.M., K.L., and M.M. were partially supported by EFree, an Energy Frontier Research Center funded by the US Department of Energy, Office of Science, Office of Basic Energy Sciences under Award Number DE-SC0001057. The x-ray scattering was conducted at the Cornell High Energy Synchrotron Source, which is supported by the National Science Foundation and the National Institutes of Health/National Institutes of General Medical Sciences under NSF award DMR-1332208. We thank Dr. Mourad Benamara from the University of Arkansas Nano-Bio Materials Characterization Facility for assistance with TEM imaging and the referees for their constructive comments regarding the manuscript.

Notes and references

1 B. Yilmaz, N. Trukhan and U. Müller, *Chin. J. Catal.*, 2012, **33**, 3–10.
2 C. T. Kresge, M. E. Leonowicz, W. J. Roth, J. C. Vartuli and J. S. Beck, *Nature*, 1992, **359**, 710–712.
3 M. E. Davis, *Nature*, 2002, **417**, 813–821.
4 A. G. Slater and A. I. Cooper, *Science*, 2015, **348**, aaa8075.
5 R. A. Mayanovic, H. Yan, A. D. Brandt, Z. Wang, M. Mandal, K. Landskron and W. A. Bassett, *Microporous Mesoporous Mater.*, 2014, **195**, 161–166.
6 C. Ducati, *Nature*, 2013, **495**, 180–181.
7 A. M. Lapeña, J. Wu, A. F. Gross and S. H. Tolbert, *J. Phys. Chem. B*, 2002, **106**, 11720–11724.
8 J. Wu, X. Liu and S. H. Tolbert, *J. Phys. Chem. B*, 2000, **104**, 11837–11841.
9 J. H. Pan and W. I. Lee, *Chem. Mater.*, 2006, **18**, 847–853.
10 K. J. Lethy, D. Beena, R. Vinod Kumar, V. P. Mahadevan Pillai, V. Ganesan and V. Sathe, *Appl. Surf. Sci.*, 2008, **254**, 2369–2376.
11 Z. Zheng, B. Yan, J. Zhang, Y. You, C. T. Lim, Z. Shen and T. Yu, *Adv. Mater.*, 2008, **20**, 352–356.
12 G. Gu, B. Zheng, W. Q. Han, S. Roth and J. Liu, *Nano Lett.*, 2002, **2**, 849–851.
13 N. Haldolaarachchige, Q. Gibson, J. Krizan and R. J. Cava, *Phys. Rev. B*, 2014, **89**, 104520.
14 D. M. Sagar, D. Fausti, S. van Smaalen and P. H. M. van Loosdrecht, *Phys. Rev. B*, 2010, **81**, 045124.
15 M. Sato, B. H. Grier, H. Fujishita, S. Hoshino and A. R. Moodenbaugh, *J. Phys. C Solid State Phys.*, 1983, **16**, 5217.
16 R. Brusetti, P. Bordet, J. Bossy, H. Schober and S. Eibl, *Phys. Rev. B*, 2007, **76**, 174511.
17 P. G. Dickens and M. S. Whittingham, *Q Rev Chem Soc*, 1968, **22**, 30–44.
18 D. Li, D. Chandra, K. Saito, T. Yui and M. Yagi, *Nanoscale Res. Lett.*, 2014, **9**, 1–8.
19 S.-H. Baeck, K.-S. Choi, T. F. Jaramillo, G. D. Stucky and E. W. McFarland, *Adv. Mater.*, 2003, **15**, 1269–1273.
20 W. Feng, G. Wu and G. Gao, *J. Mater. Chem. A*, 2014, **2**, 585–590.
21 Y. Takasu, T. Fujiwara, Y. Murakami, K. Sasaki, M. Oguri, T. Asaki and W. Sugimoto, *J. Electrochem. Soc.*, 2000, **147**, 4421–4427.
22 A. P. Hammersley, *Eur. Synchrotron Radiat. Facil. Intern. Rep. ESRF97HA02T*, 1997.
23 J. Fan, C. Yu, F. Gao, J. Lei, B. Tian, L. Wang, Q. Luo, B. Tu, W. Zhou and D. Zhao, *Angew. Chem.*, 2003, **115**, 3254–3258.
24 J.-M. Réau, C. Fouassier, G. Le Flem, J.-Y. Barraud, J.-P. Doumerc and P. Hagenmuller, *Rev. Chim. Miner.*, 1970, **7**, 975–988.
25 Y. Fujioka, J. Frantti, A. M. Asiri, A. Y. Obaid, H. Jiang and R. M. Nieminen, *J. Phys. Chem. C*, 2012, **116**, 17029–17039.
26 M. Boulova, G. Lucazeau, T. Pagnier and A. Gaskov, *J. Phys. IV*, 2001, **11**, Pr10–57–Pr10–62.
27 H. Kleinert, *Gauge fields in condensed matter: disorder fields, phase transitions; Vol. II, stresses and defects: differential geometry, crystal melting*, World Scientific, 1989.
28 Y. Xu, S. Carlson and R. Norrestam, *J. Solid State Chem.*, 1997, **132**, 123–130.
29 S. T. Anderson, S. Dey, R. A. Mayanovic, K. Landskron, M. Manik and Z. Wang, to be published.
30 M. Boulova and G. Lucazeau, *J. Solid State Chem.*, 2002, **167**, 425–434.
31 J. Chen, S. Chen, D. Lu, W. Zhang, F. Xie, W. Xie, L. Gong and C. Wang, *ChemPhysChem*, 2010, **11**, 2546–2549.
32 D. Tanaka, Y. Oaki and H. Imai, *Chem Commun*, 2010, **46**, 5286–5288.
33 A. Hussain and L. Kihlborg, *Acta Crystallogr. A*, 1976, **32**, 551–557.
34 A. J. Schultz, H. Horiuchi and H. B. Krause, *Acta Crystallogr. C*, 1986, **42**, 641–644.
35 E. Salje, *Acta Crystallogr. A*, 1975, **31**, 360–363.
36 K. P. da Silva, W. Paraguassu, M. Maczka, S. AG Filho, P. T. C. Freire and J. Hanuza, *J. Raman Spectrosc.*, 2011, **42**, 474–481.
37 I. Holclajtner-Antunović, U. B. Mioč, M. Todorović, Z. Jovanović, M. Davidović, D. Bajuk-Bogdanović and Z. Laušević, *Mater. Res. Bull.*, 2010, **45**, 1679–1684.
38 B. J. Campbell, H. T. Stokes, D. E. Tanner and D. M. Hatch, *J. Appl. Crystallogr.*, 2006, **39**, 607–614.
39 R. Dinnebier and M. Müller, *Mod. Diffr. Methods*, 2012, 27–60.
40 B. J. Campbell, J. S. O. Evans, F. Perselli and H. T. Stokes, *Ed. Newsl. No 8*, 2007, 81.
41 *TOPAS V4: General profile and structure analysis software for powder diffraction data.- User's Manual*, Bruker AXS, Karlsruhe, Germany, 2008.
42 A. P. Roberts and E. J. Garboczi, *J. Am. Ceram. Soc.*, 2000, **83**, 3041–3048.
43 S. Veprek, *J. Vac. Sci. Technol. A*, 2013, **31**, 050822.

Electronic Supporting Information

Experimental and theoretical investigation of a mesoporous K_xWO_3 material having superior mechanical strength

Sonal Dey,[*‡a] Sean T. Anderson,[a] Robert A. Mayanovic,[a] Ridwan Sakidja,[a] Kai Landskron,[b] Berenika Kokoszka,[b] Manik Mandal,[b] and Zhongwu Wang[c]

[a]*Department of Physics, Astronomy & Materials Science, Missouri State University, Springfield, MO 65897, USA.*
[b]*Department of Chemistry, Lehigh University, Bethlehem, PA 18015, USA.*
[c]*Cornell High Energy Synchrotron Source, Wilson Laboratory, Cornell University, Ithaca, NY 14853, USA.*
* sdey@sunypoly.edu
‡ *Current address: Colleges of Nanoscale Science and Engineering, State University of New York Polytechnic Institute, Albany, NY 12203, USA*

Scanning Electron Microscopy

An FEI Quanta 200 FEG Scanning Electron Microscope (SEM) was used for SEM imaging of samples of the mesoporous $K_{0.07}WO_3$ material. The energy dispersive x-ray spectroscopy measurements (SEM-EDX) were made using focused electron beam of energy 20 keV and an energy dispersive detector connected to the SEM. The SEM-EDX data and an SEM image of the mesoporous $K_{0.07}WO_3$ material are shown in Fig. 1b.

Transmission Electron Microscopy

TEM images were collected from the as-synthesized periodic FDU-12-type mesoporous $K_{0.07}WO_3$ sample at the University of Arkansas Nano-Bio Materials Characterization Facility using a Titan 80-300 with the field emission gun operated at 300 keV. The simulated selected area electron diffraction (SAED) patterns were generated from the TEM images using the fast Fourier filtering (FFT) within the imageJ software. The meso-scale ordering is clearly observed in a TEM image (Fig. 1a) of an individual sub-micron sized particle of the mesoporous $K_{0.07}WO_3$ material. Select-area energy-dispersive x-ray spectroscopy (EDX) showed the presence of K in individual sub-micron sized particles of

mesoporous $K_{0.07}WO_3$. The detection of P using EDX was prohibitive due to the strong overlap between the P K_α and W M_α emission lines.

The TEM measurements were performed on the remnants of the mesoporous K_xWO_3 sample after subjecting to pressure in the diamond anvil cell to ~ 18.5 GPa using a JEOL JEM-ARM200CF instrument operated at an accelerating voltage of 60 kV. A representative TEM image of the sample after exposing to high pressures is shown in Fig. 1c. The Fast Fourier Transform (FFT) of the TEM image (Fig. 1c inset) shows that the crystalline layered structure of the framework is preserved after subjecting the material to high pressures. The structure evident in the TEM image is consistent with the original monoclinic WO_3 phase.

SAXS Data Analysis

The face-centered cubic mesopores structure, having $Fm\bar{3}m$ symmetry group designation, was confirmed from the ratios of first: second: third peaks in the small angle x-ray scattering (SAXS) data. Details regarding application of high pressure SAXS/WAXS technique at CHESS B1/B2 beamline could be found here[S1] and the references therein. The pressure-dependent volume of the pore structure unit cell (V_P) was determined by fitting a Gaussian peak-shape to the background subtracted x-ray scattering peak occurring near 0.065 A^{-1} in Q-space (inset of Fig. 2a).[S2–S4] The fractional change in the pore-structure unit cell volume (V_P/V_0) is calculated by taking the ratio of V_P, which is the volume at pressure P, to $V_{0,}$ which is the volume at 0.1 MPa. Using a similar (Birch) equation of state functional formalism adopted by Xu et al.[S5] yields an estimate for the value of the first derivative of the bulk modulus with respect to pressure $\kappa' = 2.6(9)$ for mesoporous K_xWO_3, in good agreement with the value obtained for bulk WO_3.[S5]

Rietveld Refinement of the MAXS and WAXS Data

The "I *vs.* Q" data for the mesoporous sample and the NIST CeO_2 standard (SRM 674b) were obtained after integrating the 2D powder diffraction data using FIT2D software.[S6] The contribution to the peak shape due to the experimental setup was obtained after performing a Rietveld refinement of the CeO_2 standard. These parameters, which account for instrumental broadening of the peak shape, were kept fixed for refinement of the x-ray diffraction (i.e., the MAXS and WAXS) data from the mesoporous sample. The refinement of the x-ray diffraction (XRD) data indicate that the mesoporous $K_{0.07}WO_3$ specimen contains an orthorhombic tungsten bronze (OTB) superstructure with space group *P*222 (initial structure from ICSD 88766 but with more atoms and larger lattice constants), a Keggin-like $K_3PW_{12}O_{40}$ phase with space group $Pn\bar{3}m$ (initial structure from ICSD-165409) and an underlying monoclinic γ-WO_3 phase (initial structure from ICSD-80056) with space group $P12_1/n1$ yielding a value of R_{wp} = 6.99 and R_p = 4.63. The results of the structural refinement are summarized in Table S1. The OTB phase has lattice parameters a = 8.121(6) Å, b = 5.857(3) Å and c = 8.255(4) Å. The monoclinic unit cell of γ-WO_3 phase has lattice parameters a_m = 7.388(9) Å, b_m = 7.490(8) Å, c_m = 7.685(8) Å and β = 90.81(9)°. The cubic Keggin-like $K_3PW_{12}O_{40}$ phase has a lattice constant a_c = 11.587(2) Å. The prominent peaks corresponding to the K-bearing phases are indicated by the black vertical arrows in Fig. 3b. The monoclinic structural phase predominates in this material: the refinement yields a weight percentage composition of ~ 81.7% for the monoclinic γ-WO_3, ~ 8.1% for the OTB phase, and ~ 9.7% for the Keggin-like $K_3PW_{12}O_{40}$ phase. The remaining ~0.5% contribution is due to the reflections originating from the Rhenium gasket used in the diamond anvil cell, marked by '*' in Fig. 3b. The high intensity of the {002} triplets between Q ~ 1.6 − 1.8 $Å^{-1}$ is indicative of the presence of a predominantly monoclinic (γ-WO_3) phase which is confirmed by the refinement results. Although this could not be directly detected using TEM, it is plausible that the occurrence of the K-bearing Keggin-like $K_3PW_{12}O_{40}$ and OTB phases is highly correlated

but differentiated by the presence or lack-thereof of P, respectively, in the mesoporous material.

Rietveld refinement of the XRD data was also attempted with mixed phases of various other structures where K_xWO_3 phases with structures given by space group nos. 16, 25, 62, and 143 were attempted in combination with the γ-WO_3, $K_3PW_{12}O_{40}$ phase and the Re-impurity peaks. This additional analysis was made in order to cross check our refinement results and also to test for whether any other experimentally observed intergrowth and/or hexagonal tungsten bronzes (ITB or HTB)[S7–S12] are present in the material. We also attempted a refinement where ε-WO_3 (triclinic phase) was tried in combination with γ-WO_3, $K_3PW_{12}O_{40}$ and Re peaks. Refinement with any of these other phases did not provide satisfactory results. In the case of the absence of an additional ε-WO_3 component in the material, this result is reasonable as this phase is typically observed at low temperatures (below – 43 °C).[S13] The final refined structure with γ-WO_3 + OTB K_xWO_3 + Keggin-like $K_3PW_{12}O_{40}$ phases gives the best fit and is consistent with Raman results and TEM observations.

Table S1. Results of Rietveld Refinement of XRD data: Values of the fraction atomic coordinates (x, y, z), site occupancy, Debye-Waller factor B and the lattice parameters after Rietveld refinement of the three structures.

Keggin (SG: $Pn\bar{3}m$); a = 11.587(2) Å; V = 1555.7(8) Å^3					
Atoms	x	y	z	Site occupancy	B (Å^2)
W 1	0.527(9)	0.527(9)	0.738(2)	1.0	0.99
P 1	0.25	0.25	0.25	1.0	1.0
O 1	0.658(7)	0.658(5)	0.658(8)	1.0	1.03
O 2	0.875(5)	0.875(4)	0.002(5)	1.0	0.91
O 3	0.641(8)	0.641(5)	0.482(9)	1.0	0.95
O 4	0.437(9)	0.437(6)	0.741(9)	1.0	0.99
K 1	0.25	0.75	0.75	0.9	0.03
γ-WO_3 (SG: *P*12$_1$/*n*1); a = 7.388(9) Å; b = 7.490(8) Å; c = 7.685(8) Å; β = 90.81°(9); V = 425.3(2) Å^3					
W 1	0.239(9)	0.049(8)	0.296(9)	1.0	0.92
W 2	0.255(7)	−0.006(9)	0.769(7)	1.0	0.91
O 1	0.001(1)	0.037(7)	0.212(5)	1.0	0.95
O 2	−0.003(2)	0.463(5)	0.216(8)	1.0	0.97
O 3	0.282(5)	0.260(3)	0.287(9)	1.0	0.99

O 4	0.211(7)	0.260(5)	0.731(6)	1.0	0.96
O 5	0.286(3)	0.039(7)	0.006(3)	1.0	0.99
O 6	0.285(4)	0.485(8)	−0.008(3)	1.0	1.01
OTB (SG:*P*222); a = 8.121(6) Å; b = 5.857(3) Å; c = 8.255(4) Å; V = 392.6(4) Å^3					
K 1	0.5	0.285(6)	0.5	1.0	1.0
W 1	0.5	0	0	1.0	1.0
W 2	0.5	0.5	0	1.0	1.0
W 3	0.872(5)	−0.014(9)	0.223(9)	1.0	0.98
W 4	0.800(5)	0.437(9)	0.217(9)	1.0	0.95
O 1	0.85	0	0	1.0	0.92
O 2	0.85	0.5	0	1.0	0.91
O 3	0	0	0.3	1.0	0.99
O 4	0	0.5	0.3	1.0	0.97
O 5	0.64	0	0.18	1.0	0.96
O 6	0.64	0.5	0.18	1.0	0.95
O 7	0.79	0	0.5	1.0	0.94
O 8	0.79	0.5	0.5	1.0	0.97
O 9	0.5	0.25	0	1.0	0.93
O 10	0.8	0.25	0.25	1.0	0.99
O 11	0.8	0.75	0.25	1.0	0.91

Raman Measurements and Analysis

Measurements of the vibrational phonon modes were made using a Horiba LabRAM HR800 micro Raman setup and a 50mW 532 nm narrow bandwidth solid-state laser source. Filters were put in place to lower the intensity of the incident light on the sample and Stokes Raman excitation lines were measured in the experiments. Our fitting of the Raman spectrum measured from the as prepared mesoporous $K_{0.07}WO_3$ is shown in Fig. S1 and the results are summarized in Table S2. Multiple pseudo-Voigt peak shapes were used in order to determine the peak positions and peak widths in the Raman spectrum.[S14]

Table S2. Peak positions, widths and types after peak-fitting of Raman spectrum: Fitting of the Raman results. Values of the fitting parameters using pseudo-Voigt peak shapes for the plot of Fig. S1 are tabulated. Here, w is the peak width, x_c is the peak center and the value of m determines the pseudo Voigt line-shapes: m = 0 means pure Gaussian and m = 1 implies pure Lorentzian line-shape.

Peak no.	x_c (cm^{-1})	w (cm^{-1})	m
1	65.1 ± 0.2	10.1 ± 0.4	0
2	85.8 ± 0.9	17.9 ± 2.5	0
3	132.1 ± 0.3	16.8 ± 0.8	1
4	197.6 ± 1.1	37.8 ± 2.9	0
5	264.6 ± 0.6	38.9 ± 1.5	1
6	294.8 ± 3.0	33 ± 12.3	1
7	323.0 ± 3.4	32.4 ± 9.3	0
8	367.0 ± 3.8	31.5 ± 10.0	0
9	427.0 ± 2.6	40.5 ± 7.1	0
10	648.0 ± 1.0	96.3 ± 2.0	1
11	700.6 ± 0.3	49.1 ± 1.1	1
12	802.7 ± 0.1	29.8 ± 0.1	1
13	989.0 ± 1.9	5.3 ± 3.2	1
14	1004.0 ± 1.2	7.3 ± 2.8	1
15	1141.0 ± 2.2	105.0 ± 9.0	1

Table S3 shows the Raman band values from measurements made on the periodic FDU-12 type mesoporous $K_{0.07}WO_3$ sample in comparison to the Raman shifts observed by da Silva *et al.*[S15] from measurements of a bulk $Cs_4W_{11}O_{35}$ hexagonal tungsten bronze, along with the vibrational mode assignments made from lattice dynamics theory.[S15] The incorporation of alkali ions (Li^+ and H^+) has been observed to cause distortion of the octahedral units and W^{6+} reduction to W^{5+} in bulk M_xWO_3, giving rise to W^{5+}–O and W^{5+}=O bending modes close to 330 cm^{-1} and 450 cm^{-1}.[S16] It seems reasonable that the incorporation of the K^+ ion would cause similar effects in mesoporous $K_{0.07}WO_3$.

Table S3. Comparison of Raman bands of K_xWO_3 with literature: A comparison of the predominant WO_3 Raman band values and those attributed to the OTB phase measured from our mesoporous $K_{0.07}WO_3$ to the Raman bands measured by da Silva *et al.* from a $Cs_4W_{11}O_{35}$ hexagonal tungsten bronze.[S15] The vibrational mode assignments made from lattice dynamics theory by Da Silva *et al.* [S15] are also included.

Our Study (cm^{-1})	Da Silva et al. (cm^{-1})	Vibrational mode (as assigned by da Silva et al.[S15])
803	799	Apical O vibration within WO_6 octahedra
701	718-719	Apical O vibration within WO_6 octahedra
648	651	O stretching mode in plane of hexagonal ring of WO_6 octahedra
427	414	O-W-O bending modes in plane of hexagonal ring of WO_6 octahedra
367	360	Hex ring O-W-O bending modes + librations of WO_6 octahedra

UV-Vis Measurements

A suspension of the mesoporous FDU-12-type $K_{0.07}WO_3$ was prepared in DI water and allowed to evaporate on an ordinary microscope glass slide to create a film of the material. The UV-Vis transmission/absorption spectra (with the glass slide used as a reference) of the mesoporous $K_{0.07}WO_3$ film were measured using an Ocean Optics HR 4000 spectrophotometer and the OceanView 1.4 acquisition software. A fiber-optic coupled DT-Mini-2 deuterium/tungsten-halogen lamp source (Ocean Optics) was used for light excitation of the sample. The OceanView 1.4 acquisition software enables collection of spectral readings on an instantaneous basis: The accumulated spectra were collected in ~3 ms. The transmission spectral measurements were repeated several times to ensure collection of reproducible data. The energy gap of mesoporous $K_{0.07}WO_3$ is estimated from the intersection of the fitted line of the $(\alpha \cdot h\nu)^{1/2}$ quantitity at the zero point with the energy ($h\nu$) axis as shown in Fig S2.

N_2 Sorption Measurements

The N_2 sorption measurements of the mesoporous $K_{0.07}WO_3$ material were made using a Quantachrome Autosorb-1 gas-sorption analyzer. The samples were degassed in vacuum at

150 °C overnight prior to the N_2 sorption measurements. The specific surface area of the sample was calculated using the Brunauer-Emmett-Teller (BET) method. The results of the N_2 sorption measurements along with the corresponding DFT pore-size distribution of the mesoporous K_xWO_3 material are shown in Fig. S3. DFT calculations gave an estimate of the total pore volume as 0.6 cm^3/g and a narrow pore-size distribution with the pore width to be approximately 12.5 nm. This is in reasonable agreement, within experimental errors, with the TEM measurements of Fig. 1a.

Ab Initio Calculations

The bulk modulus (κ) of various WO_3 and K-bearing WO_3 phases were calculated using *ab-initio* molecular dynamics (AIMD) simulations within the Density Functional Theory (DFT) approximation as implemented in VASP.[S17,S18] The approach implemented in VASP is based on a finite-temperature local-density approximation and an exact evaluation of the instantaneous electronic ground state at each MD-step.[S17,S18] The AIMD simulations were performed with a 2 fs time step. We employed gamma point sampling and the projected augmented wave (PAW)[S19] potentials with the GGA-PBE[S20] exchange and correlation approximations. A constant energy cut-off of 500 eV was used and the electronic convergence was set to 10^{-4} eV to ensure a high precision on the average volume/pressure values. The bulk modulus values were calculated from the relaxed unit cell volume dependence on pressure using NVT/NPT simulations. Using a similar methodology as in the case of the pressure-dependent small angle x-ray scattering (SAXS) experiments, the bulk modulus was estimated by taking the inverse slope of a linear relationship of the fractional change in the unit cell volume (V_P/V_0) with pressure, where V_P and V_0 are the volumes at high and ambient pressure, respectively. For molecular dynamics simulations of a periodic mesoporous WO_3, a WO_3 monoclinic unit cell was assembled and then relaxed by density functional theory (DFT) calculations at three different pressures (0.1, 2.8 and 4.6 GPa). This was necessary in order to

properly account for torsional buckling of the WO_6 polyhedra in monoclinic WO_3 under pressure. The monoclinic unit cells, relaxed at each pressure, were repeated to form cubes (28 nm on each side) of about 1.5 million atoms. Pores were carved out in a face-centered cubic arrangement, with a variety of pore sizes to control porosity. LAMMPS software[S21] was used in conjunction with Buckingham potentials for W and O[S22] to make the molecular dynamics (MD) simulations. Hydrostatic pressure was applied to the porous blocks until an equilibrium volume was reached. The bulk moduli were determined from the linear trend of V_P/V_0 with pressure, where V is the volume of the simulation cell. By repeating this procedure for simulation boxes having varying pore volumes, the effect of porosity on the bulk modulus was determined using MD simulations. Additional details on methods and procedures are given in the Supplementary Information.

The AIMD results for the calculation of the bulk modulus of monoclinic, orthorhombic, and hexagonal WO_3 as well as hexagonal $K_{0.33}WO_3$, are shown in Table S4. The bulk modulus was calculated for the Keggin $K_3PW_{12}O_{40}$ cubic structure as follows: First, the elastic coefficients (c_{ij}) were calculated at the ground state by use of strain-stress analysis[S23] and AIMD simulations. The structure was initially fully relaxed and subsequently a small strain was applied to each independent ε_j strain element. The six stress component σ_{ij} were calculated from the strain following the set of linear elastic equations:

$$\sigma_{ij} = \sum_{ij} c_{ij} \varepsilon_j$$

For a cubic crystal structure, the bulk modulus (κ) can be calculated from the elastic constants using $\kappa = (2\ C_{12} + C_{11})/3$. We applied a full occupancy with respect to all of the atomic positions for the Keggin structure: The calculated bulk modulus value (κ = 37.5 GPa) should be treated as an upper estimate.

Table S4. AIMD results: Bulk modulus values calculated using AIMD for various WO_3 and K-bearing WO_3 phases.

System	Space Group	Bulk modulus (GPa)
Monoclinic WO_3	P121/n1	50.7
Orthorhombic WO_3	P222	132.8
Hexagonal WO_3	P6/mmm	171.7
Hexagonal $K_{0.33}WO_3$	P6/mmm	194.1

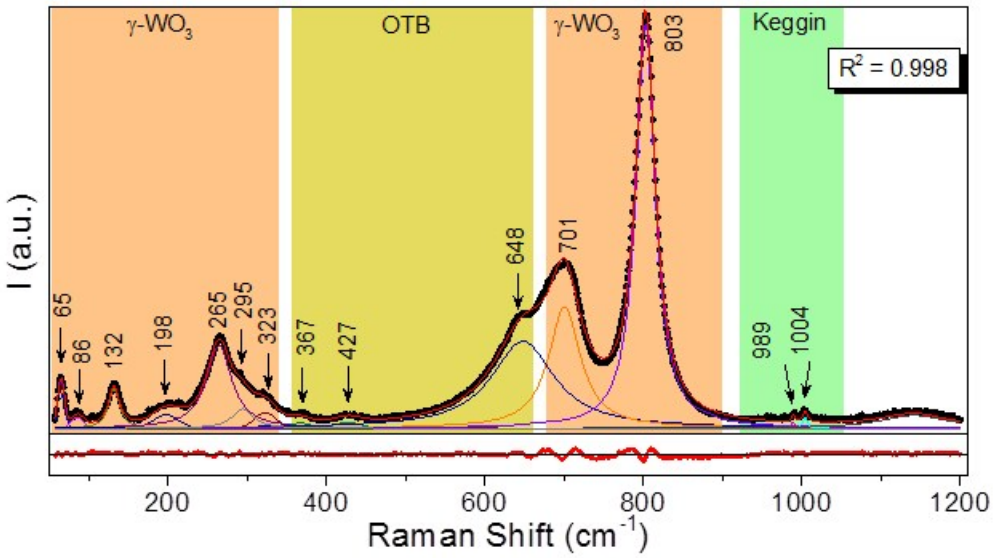

Fig. S1. Peak-fitting of Raman Spectrum: Peak fitting of the Raman spectrum measured from the as prepared mesoporous $K_{0.07}WO_3$. The spectrum was fit with combinations of multiple pseudo Voigt peak shapes. The coefficient of determination ($R^2 = 0.998$) of the fit is noted in the Figure and the peak positions (rounded to zero decimal point) are also shown. Table S3 gives the details of the fitting parameters.

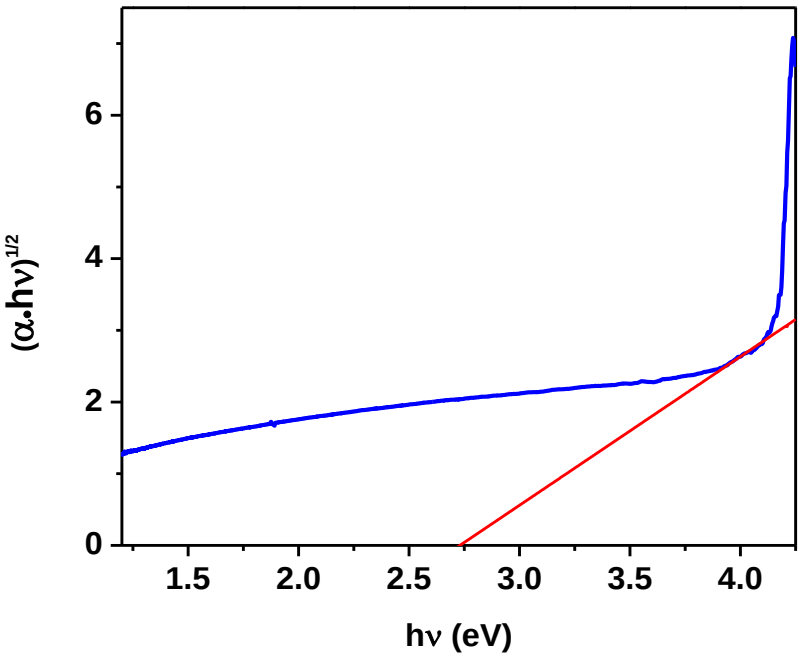

Fig. S2 The $(\alpha \cdot h\nu)^{1/2}$ quantitity vs photon energy ($h\nu$) as determined from the UV-Vis absorption data measured (at room temperature) from mesoporous $K_{0.07}WO_3$. The extrapolated fitted line intersects the energy axis at ~2.7 eV.

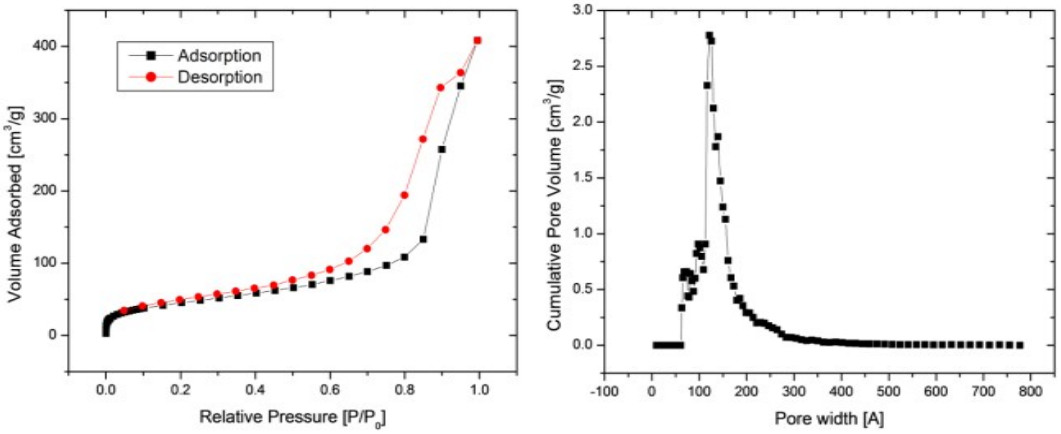

Fig. S3 (a) N_2 adsorption-desorption isotherms and (b) pore volume as a function of pore width of mesoporous $K_{0.07}WO_3$. The data were collected on a sample etched in 10% HF for ~6 hours.

References

S1. T. Wang, R. Li, Z. Quan, W. S. Loc, W. A. Bassett, H. Xu, Y. C. Cao, J. Fang and Z. Wang, *Adv. Mater.*, 2015, **27**, 4544–4549.

S2. R. A. Mayanovic, H. Yan, A. D. Brandt, Z. Wang, M. Mandal, K. Landskron and W. A. Bassett, *Microporous Mesoporous Mater.*, 2014, **195**, 161–166.

S3. A. M. Lapeña, J. Wu, A. F. Gross and S. H. Tolbert, *J. Phys. Chem. B*, 2002, **106**, 11720–11724.

S4. J. Wu, X. Liu and S. H. Tolbert, *J. Phys. Chem. B*, 2000, **104**, 11837–11841.

S5. Y. Xu, S. Carlson and R. Norrestam, *J. Solid State Chem.*, 1997, **132**, 123–130.

S6. A. P. Hammersley, *Eur. Synchrotron Radiat. Facil. Intern. Rep. ESRF97HA02T*, 1997.

S7. P. G. Dickens and M. S. Whittingham, *Q Rev Chem Soc*, 1968, **22**, 30–44.

S8. A. Hussain and L. Kihlborg, *Acta Crystallogr. A*, 1976, **32**, 551–557.

S9. T. Wolfram and S. Ellialtioglu, *Electronic and optical properties of d-band perovskites*, Cambridge University Press Cambridge, 2006.

S10. M. Johnsson and P. Lemmens, *Crystallography and chemistry of perovskites*, John Wiley & Sons Ltd, Chichester, UK, 2007, vol. 4.

S11. A. Hussain, *Acta Chem Scand A*, 1978, **32**.

S12. R. Sharma and L. Kihlborg, *Mater. Res. Bull.*, 1981, **16**, 377–380.

S13. E. Salje, *Ferroelectrics*, 1976, **12**, 215–217.

S14. G. K. Wertheim, M. A. Butler, K. W. West and D. N. E. Buchanan, *Rev. Sci. Instrum.*, 1974, **45**, 1369–1371.

S15. K. P. da Silva, W. Paraguassu, M. Maczka, S. AG Filho, P. T. C. Freire and J. Hanuza, *J. Raman Spectrosc.*, 2011, **42**, 474–481.

S16. S.-H. Lee, H. M. Cheong, C. E. Tracy, A. Mascarenhas, D. K. Benson and S. K. Deb, *Electrochimica Acta*, 1999, **44**, 3111–3115.

S17. G. Kresse and J. Furthmüller, *Comput. Mater. Sci.*, 1996, **6**, 15–50.

S18. G. Kresse and J. Furthmüller, *Phys. Rev. B*, 1996, **54**, 11169.

S19. P. E. Blöchl, *Phys. Rev. B*, 1994, **50**, 17953.

S20. J. P. Perdew, K. Burke and M. Ernzerhof, *Phys. Rev. Lett.*, 1996, **77**, 3865.

S21. S. Plimpton, *J. Comput. Phys.*, 1995, **117**, 1–19.

S22. M. S. Islam, S. Lazure, R. Vannier, G. Nowogrocki and G. Mairesse, *J. Mater. Chem.*, 1998, **8**, 655–660.

S23. O. H. Nielsen and R. M. Martin, *Phys. Rev. Lett.*, 1983, **50**, 697.